Control of the Effective Free-Energy Landscape in a Frustrated Magnet by a Field Pulse

Yuan Wan[1,*] and Roderich Moessner[2]
[1]Perimeter Institute for Theoretical Physics, Waterloo, Ontario N2L 5G7, Canada
[2]Max Planck Institute for the Physics of Complex Systems, 01187 Dresden, Germany
(Received 22 May 2017; published 19 October 2017)

Thermal fluctuations can lift the degeneracy of a ground state manifold, producing a free-energy landscape without accidentally degenerate minima. In a process known as order by disorder, a subset of states incorporating symmetry breaking may be selected. Here, we show that such a free-energy landscape can be controlled in a nonequilibrium setting as the slow motion within the ground state manifold is governed by the fast modes out of it. For the paradigmatic case of the classical pyrochlore XY antiferromagnet, we show that a uniform magnetic field pulse can excite these fast modes to generate a tunable effective free-energy landscape with minima at thermodynamically unstable portions of the ground state manifold.

DOI: 10.1103/PhysRevLett.119.167203

The emergence of a thermodynamic landscape from microscopic interactions, and its consequences for macroscopic behavior, is a central theme of condensed matter physics. The essential role of fluctuation contributions to the free-energy landscape is underlined by entropic interactions in soft matter [1–3], infinite temperature phase transitions [4,5], and, at low temperatures, the phenomenon of order by disorder (OBD) [6–10].

This raises the question of how one can control a free-energy landscape in a condensed matter system by manipulating fluctuations instead of changing its Hamiltonian. In equilibrium (EQ), the Boltzmann distribution fully dictates the free-energy landscape and hence allows little room for control. In this work, we show that such control is feasible if one drives the system out of equilibrium, where fluctuations dynamically produce a free-energy landscape that may be tuned by changing the nonequilibrium conditions.

To illustrate this, we sketch a simple but generic scenario. It is based on a crisp distinction between energetic and entropic contributions to the free energy as exists at low energies in a broad class of geometrically frustrated magnets. This arises because geometrical frustration often results in an accidentally degenerate ground state (GS) manifold, i.e., a large, continuous family of degenerate GSs not related by any symmetry operation. In EQ, the entropy due to the thermal fluctuations near each GS can vary along the manifold. Parametrizing the ground state manifold by coordinates $\mathcal{Q}$, one thus obtains an effective free energy $V(\mathcal{Q})$ from integrating out the fluctuations, which can thus lift the accidental degeneracy and tend to stabilize the GS(s) with maximal entropy.

We focus on systems with Hamiltonian dynamics such as frustrated vector spin models. We separate variables into the pseudo-Goldstone modes describing the drift motion within the GS manifold, and the other normal modes involving deviations out of it (Fig. 1) [11]. In the low temperature limit, the drift motion within the GS manifold is vanishingly slow as they experience no linear restoring force. By contrast, the other modes are fast owing to their finite stiffness. Integrating these out (a controlled procedure provided their frequencies are bounded above 0) yields a nonequilibrium contribution to the effective free energy of the form $V(\mathcal{Q}) \propto \sum_i I_i \sqrt{K_i(\mathcal{Q})}$, with $I_i > 0$ being the action variable of the ith excited normal mode, and K_i being its $\mathcal{Q}$-dependent stiffness [12]. Importantly, $V(\mathcal{Q})$ can be tuned by adjusting the weights I_i. This we show can be achieved straightforwardly by a magnetic field pulse.

We flesh out this scenario with a concrete model, for which we establish properties of the effective landscape, its tunability and resulting dynamics, as well as its interplay with the thermal fluctuations. We also develop an analytic toy model that transparently explains the central phenomenon.

Consider the classical pyrochlore XY antiferromagnet, which has gained prominence thanks to its likely realization of OBD in the rare earth magnet $Er_2Ti_2O_7$ [13–20],

$$H = \sum_{\langle ij \rangle} -\frac{J_\pm}{2}(S_i^+ S_j^- + \text{H.c.}) + \frac{J_{\pm\pm}}{2}(e^{i\psi_{ij}} S_i^+ S_j^+ + \text{H.c.}) - J^{zz} S_i^z S_j^z. \quad (1)$$

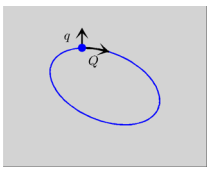

FIG. 1. Geometrical frustration for vector spins produces an accidentally degenerate GS manifold (blue ellipse) in many-body configuration space (gray box). $\mathcal{Q}$ parametrizes the GS manifold, and q the fluctuations out of it.

Here, spin $\mathbf{S}_i$ of length S resides on pyrochlore lattice site i. The summation runs over nearest-neighbor bonds. $S_i^{x,y,z}$ are the Cartesian components of the spin in the local frame $\{\hat{x}_i, \hat{y}_i, \hat{z}_i\}$, and $S_i^{\pm} \equiv S^x \pm iS_i^y$. ψ_{ij} are bond-dependent phase angles due to local spin frames (see [21] for details). $J_{\pm}$, J_{zz} parametrize anisotropic Heisenberg exchange interaction, whereas $J_{\pm\pm}$ originates from a Dzyaloshinskii-Moriya or pseudodipolar interaction. We assume $J_{\pm} > J_{\pm\pm}$, $J_{zz} > 0$. For simplicity, we have omitted a symmetry-allowed term known as $J_{z\pm}$ as it will not change the physics discussed in this work.

We briefly review the OBD following from Eq. (1) [15–20]. The GSs, which preserve lattice translation symmetry, show Néel order with complex order parameter $O \equiv \sum_i S_i^+/(\mathcal{N}S)$ ($\mathcal{N}$ is the number of sites). GS spin configurations are $\mathbf{S}_i = S(\cos\phi\hat{x}_i + \sin\phi\hat{y}_i)$ with $\phi = \arg O$ [Fig. 2(a)]. Crucially, the GS energy is independent of ϕ: Eq. (1) possesses an accidental $U(1)$ degeneracy although it only exhibits discrete symmetries.

At small but finite temperature, the entropy due to the spin wave fluctuations lifts the accidental degeneracy, yielding six symmetry-equivalent maxima known as ψ_2 states, located at $\phi = m\pi/3$, $m \in \mathbb{Z}$: thermal OBD corresponds to an emergent entropic six-state clock anisotropy in the $U(1)$ manifold.

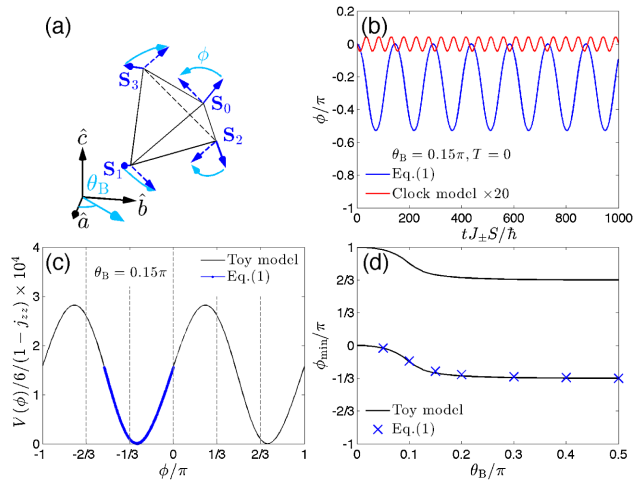

FIG. 2. (a) GS of Eq. (1) in a unit cell. 0–3 label the sublattices. Starting from a GS (blue solid arrows, corresponding to $\phi = 0$), one obtains another GS (blue broken arrows, $\phi = \pi/2$) by rotating all spins with respect to their local threefold axes. Inset: Crystallographic axes (black arrows), pulse polarization (light blue arrow), and polarization angle θ_B. (b) GS Néel order parameter argument ϕ as a function of time t after a pulse with polarization angle $\theta_B = 0.15\pi$. Results from the simulation of Eq. (1) (blue) contrasted to a model with an inherently energetic (rather than emergent entropic) clock term (red). (c) Effective potential energy density $V(\phi)/[6(1-j_{zz})]$ in the GS manifold from the toy model (black) and the model simulation in (b) (blue). Gray dashed lines mark the positions of ψ_2 states. (d) Potential minima $\phi_{\min}$ as a function of pulse polarization angle θ_B. Black solid lines show the two degenerate minima predicted by the toy model. Blue crosses mark the center position of the ϕ oscillation extracted from simulation.

To study the non-EQ dynamics of Eq. (1), we endow the spins with precessional Landau-Lifshitz (LL) dynamics. We begin with a toy model that captures the essential features: taking the spins on each of the four sublattices $i = 0$–3 with the same orientation, $\mathbf{S}_i/S = \sqrt{1-z_i^2}(\cos\phi_i\hat{x} + \sin\phi_i\hat{y}) + z_i\hat{z}_i$, reduces the degrees of freedom to the four spins in a unit cell. In other words, we freeze spin wave modes with wave vector $\mathbf{k} \neq 0$.

We define $\phi \equiv (\phi_0 + \phi_1 + \phi_2 + \phi_3)/4$, $\phi_a \equiv (\phi_0 + \phi_1 - \phi_2 - \phi_3)/2$, $\phi_b \equiv (\phi_0 + \phi_2 - \phi_1 - \phi_3)/2$, and $\phi_c \equiv (\phi_0 + \phi_3 - \phi_1 - \phi_2)/2$, along with corresponding z and $z_{a,b,c}$. ϕ corresponds to the pseudo-Goldstone mode, whereas $\phi_{a,b,c}$ correspond to finite-frequency optical magnons. Linearizing Eq. (1) in $\phi_{a,b,c}$ yields [21]

$$\ddot{\phi}_l = -\omega_0^2 f_l(\phi)\phi_l^2; \quad \ddot{\phi} = -\tilde{\omega}_0^2 \sum_{l=a,b,c} \phi_l^2 \sin(2\phi + \Theta_l), \tag{2}$$

with rescaled variables such that $J_{\pm}S \to 1$, $j_{\pm\pm} \equiv J_{\pm\pm}/J_{\pm}$, $j_{zz} \equiv J_{zz}/J_{\pm}$. l runs over labels a, b, c. $f_l(\phi) = 1 - j_{\pm\pm}/2\cos(2\phi + \Theta_l)$. $\Theta_a \equiv 0$, $\Theta_b \equiv 2\pi/3$, and $\Theta_c \equiv -2\pi/3$. $\omega_0 \equiv 4\sqrt{3 + j_{zz}}$ and $\tilde{\omega}_0 \equiv \sqrt{6j_{\pm\pm}(1 - j_{zz})}$ are constant frequencies.

Since $\phi_l \ll 1$, the optical magnons are fast harmonic oscillators parametrically driven by the slow motion of the pseudo-Goldstone mode ϕ. We thus proceed to integrate out optical magnons by using the method of averaging [12,22]. We obtain [21] $\ddot{\phi} = -\partial V(\phi)/\partial\phi$, where

$$V(\phi) = \frac{3(1 - j_{zz})}{\sqrt{3 + j_{zz}}} \sum_{l=a,b,c} I_l \sqrt{f_l(\phi)} \tag{3}$$

is the effective potential in the $U(1)$ degenerate manifold. I_l, the action variable of mode l, is an adiabatic invariant [23], so that $V(\phi)$ is approximately time independent.

For $I_a = I_b = I_c$, $V(\phi) \propto -j_{\pm\pm}^3\cos(6\phi) + o(j_{\pm\pm}^3)$ with minima at the states selected by OBD in EQ. For generic values of $I_{a,b,c}$, however, the minima are twofold degenerate, $V(\phi) = V(\phi + \pi)$ and, crucially, located elsewhere.

Selectively exciting optical magnons thus permits control of the individual values of $I_{a,b,c}$ and thereby $V(\phi)$. This can in fact be achieved simply via the polarization of an applied magnetic field pulse. To see this, note that the magnetization $M_{a,b,c}$ along the crystallographic a, b, c axes, to leading order in $\phi_{a,b,c}$ and $z_{a,b,c}$, is [21,24]

$$\frac{M_{a,b,c}}{\mathcal{N}\mu_B S} = -\frac{2g_{\parallel}}{\sqrt{3}} z_{a,b,c} - \frac{4g_{\perp}}{\sqrt{6}} \sin(\phi - \Theta_{a,b,c})\phi_{a,b,c}, \tag{4}$$

with $g_{\parallel}(g_{\perp})$ being the Landé g factor along the local $\hat{z}$ axis ($\hat{x}$, $\hat{y}$ axes): the a, b, c magnons respectively carry magnetic dipole moments in the three crystallographic axes.

We next confirm numerically such generation and control of an effective free-energy landscape. We first equilibrate the model at temperature T and then apply a short magnetic pulse whose temporal profile is a Dirac-δ function: $\mathbf{B}(t) = B_{\max}\hat{n}\delta(t/\tau)$, where $B_{\max}$ is the peak strength, τ is the duration, and $\hat{n}$ is the polarization. After the pulse, we remove the bath and let the system evolve according to the LL equation at $t > 0$.

The simulation uses a periodic lattice of $8 \times 8 \times 8$ unit cells. We do not observe significant system size dependence in dynamics [21]. We integrate the LL equation via the fourth order Runge-Kutta method (RK4). For nonzero T, we generate 2^{10} initial states for the LL equation from canonical Monte Carlo calculations and average over microcanonical trajectories. The RK4 step width is chosen such that the relative error of energy $\epsilon < 10^{-5}$. The integration stops at $10^3\hbar/(J_\pm S)$, corresponding to $>10^3$ oscillation cycles of optical magnons. Model parameters $j_{\pm\pm} = 0.646$, $j_{zz} = 0.192$, $g_\parallel = 2.45$, and $g_\perp = 6.0$ are similar to those for $Er_2Ti_2O_7$ [16]. In EQ, the ψ_2 states occur with equal probability. We assume the model is initially in a single domain with $\phi = 0$. Only the area of the δ peak $B_{\max}\tau$ enters the equation of motion, which we set to 0.1 ps · T [21]. The pulse polarization lies in the ab plane, i.e., $\hat{n} = \cos\theta_B\hat{a} + \sin\theta_B\hat{b}$ [Fig. 2(a), inset]. In this setup, the pulse only excites a and b magnons. The energy deposited by the pulse is $\sim 10^{-3}\ J_\pm S^2$ per spin.

First consider the $T = 0$ limit. ϕ initially rests at 0 for $t < 0$. The pulse generates a $V(\phi)$ whose minima are located elsewhere. ϕ thus oscillates around a nearby minimum of $V(\phi)$ [see Fig. 2(b) for $\theta_B = 0.15\pi$]. To extract $V(\phi)$ from simulation, we use the conservation of energy [21], $V(\phi)/[6(1 - j_{zz})] + K = \text{const.}$, where the first and second terms are respectively the potential and kinetic energy density of the pseudo-Goldstone mode. K can be evaluated from data. The result is in good agreement with Eq. (3), with $I_{a,b,c}$ extracted from the initial condition [Fig. 2(c)].

We next show that the accidental degeneracy underpinning OBD is constitutive to the controllability of the free-energy landscape in our present scheme. To do this, we contrast Eq. (1) with a clock model where OBD is mimicked by microscopic interactions yielding the same degeneracy lifting [25]: we add a six-state clock anisotropy term, $-\Delta/S^4[(S_i^+)^6 + \text{H.c.}]$, to Eq. (1) and set $j_{\pm\pm} = 0$. For the clock model, $V(\phi) \propto -\Delta\cos(6\phi)$, and the pulse only produces a small renormalization of Δ: for $\Delta/J_\pm = 10^{-4}$, ϕ oscillates around 0 [Fig. 2(b)]. The oscillation amplitude is small as the Néel order couples to the magnetic field nonlinearly.

We further demonstrate the control on $V(\phi)$ by scanning the field polarization $\hat{n}$. As $\hat{n}$ rotates from the a to the b axis, I_b increases while I_a decreases. The I_a term of Eq. (3) favors $\phi = 0$, π, whereas the I_b term favors $\phi = -\pi/3$, $2\pi/3$. Thus, the minimum positions $\phi_{\min}$ continuously shift from 0, π to $-\pi/3$, $2\pi/3$. In numerical simulation, the shift of $\phi_{\min}$ is manifest as the change of the center position of ϕ oscillation [Fig. 2(d)]. The small discrepancy between the toy model and the simulation is likely due to nonlinear effects neglected in Eq. (2).

At nonzero temperature, the effective potential produced by optical magnons is also subject to the thermal fluctuations in $\mathbf{k} \neq 0$ modes. In EQ, these modes produce an entropic effective potential with the magnitude of $\sim 10^{-3}k_BT$ per spin. We now show that the above non-EQ phenomena are nonetheless robust at low T. We start with $k_BT/(J_\pm S^2) = 10^{-3}$. Figures 3(a) and 3(b) show two representative cases. For $\theta_B = 0.1\pi$, $\arg\langle O\rangle$, the argument of the average Néel order parameter, exhibits a persistent oscillation with small damping. On the other hand, for $\theta_B = 0.5\pi$, in addition to oscillation in the argument, the modulus $|\langle O\rangle|$ decreases quickly. However, the Néel order persists as the average modulus squared $\langle|O|^2\rangle \approx 1$ within the simulation time window [Fig. 3(b)]. Thus, the decrease in $|\langle O\rangle|$ is due to the loss of anisotropy; i.e., the argument of O explores the $U(1)$ degenerate manifold. This is made clear by the histogram of $\arg O$ for $\theta_B = 0.5\pi$, which spreads out in the $U(1)$ manifold at late time [Fig. 3(d)].

The difference between these two types of behavior originates dynamically as follows. Consider the a and b magnons underpinning $V(\phi)$. Their ensemble-averaged action variables $\langle I_{a,b}\rangle$ gradually decay in time, indicating

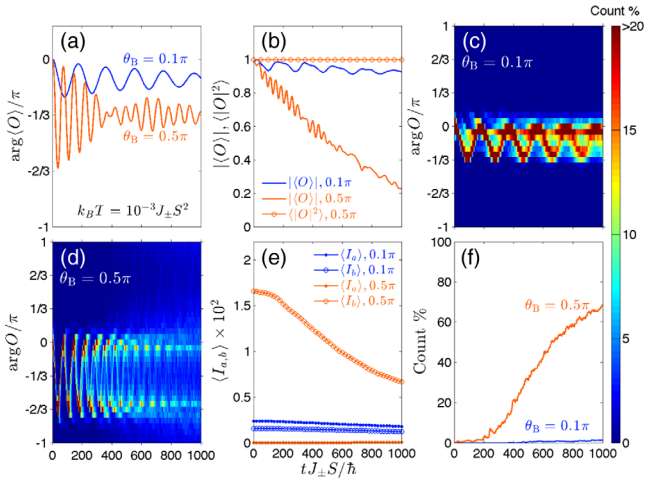

FIG. 3. (a) Argument and (b) modulus of the ensemble-averaged complex Néel order parameter $\langle O\rangle$ as a function of time t at $k_BT = 10^{-3}\ J_\pm S^2$. Blue and orange lines are for pulse polarization angles $\theta_B = 0.1\pi$ and 0.5π, respectively. (b) also shows the ensemble average of modulus squared, $\langle|O|^2\rangle$, for $\theta_B = 0.5\pi$ (orange open circles). (c)(d) Histogram of the Néel order parameter argument $\arg O$ as function of time t at the same temperature. (e) Same as (a) but for ensemble average of action variables I_a (dots) and I_b (open circles) associated with the optical magnons a and b. (f) Number of trajectories for which the total energy of the pseudo-Goldstone mode exceeds the potential maxima.

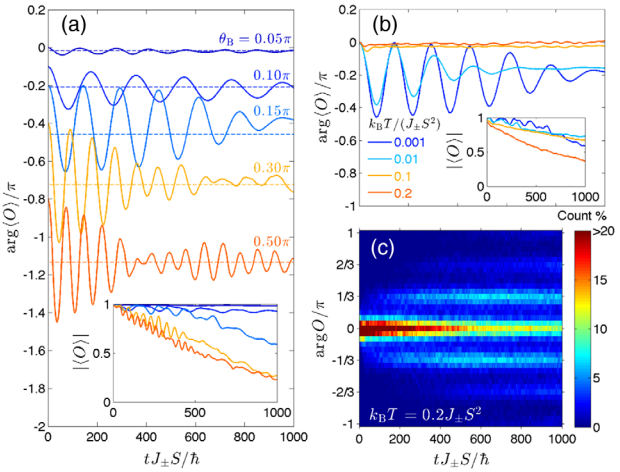

FIG. 4. (a) Argument and modulus (inset) of the ensemble-averaged Néel order parameter $\langle O\rangle$ versus time t for various pulse polarizations at $k_BT = 10^{-3}\ J_\pm S^2$. $\arg\langle O\rangle = 0$ at time $t = 0$, but plots are shifted vertically for visibility. Dashed lines mark the predicted effective potential minima from the toy model. (b) Same as (a) but for fixed pulse polarization angle $\theta_B = 0.15\pi$ at four different temperatures. (c) Histogram of Néel order parameter argument $\arg O$ as a function of time t for $\theta_B = 0.15\pi$ at $k_BT = 0.2\ J_\pm S^2$.

that the energy is being slowly transferred to other modes [Fig. 3(e)]. Note that $I_{a,b,c}$ must equalize and ϕ must return to ψ_2 positions after the thermal equilibration time $\tau_{\rm eq}$. Yet, the persistent difference in $I_{a,b}$ indicates $\tau_{\rm eq} > 10^3\hbar/J_\pm S$. Comparing $\langle I_{a,b}\rangle$ for $\theta_B = 0.1\pi$ with $\theta_B = 0.5\pi$, the latter exhibits a more pronounced decrease. This slow decay implies that of $V(\phi)$ as well [Eq. (3)]. Now, the motion of the pseudo-Goldstone mode ϕ is oscillatory as long as its total energy E is less than the potential maxima $V_{\rm max}$. As $V_{\rm max}$ decreases, ϕ may therefore overcome the potential barrier and enter an open orbit. As a qualitative test of this picture, we extract E and $V_{\rm max}$ from data and count the number of trajectories for which $E > V_{\rm max}$ [Fig. 3(f)]. For $\theta_B = 0.1\pi$, the number of such trajectories is negligible, whereas the count steadily grows in time for $\theta_B = 0.5\pi$.

Having gained a qualitative understanding of the two representative cases, we consider the systematic θ_B dependence of the order parameter dynamics [Fig. 4(a)]. Throughout, $\arg\langle O\rangle$ exhibits damped oscillation, while $|\langle O\rangle|$ decreases at a larger rate as θ_B approaches $\pi/2$. Similar to $T = 0$, the center of $\arg\langle O\rangle$ oscillation gradually shifts from 0 to $-\pi/3$. The center position at early times agrees with the potential minima of Eq. (3) with $I_{a,b,c}$ extracted from initial conditions. The small drift in oscillation center at late time is due to a small change in the relative weight of $I_{a,b,c}$ and the increasing importance of thermal fluctuations. The higher oscillation frequency at larger θ_B results from the larger curvature of $V(\phi)$. The beating of the $\arg\langle O\rangle$ observed at $\theta_B = 0.5\pi$ is likely due to a finite-width distribution of the oscillation frequencies.

Finally, we study the temperature dependence of this phenomenon. Figure 4(b) shows the order parameter dynamics for fixed $\theta_B = 0.15\pi$. Damping of the oscillation in $\arg\langle O\rangle$ increases with temperature T, while the oscillation center moves toward 0. Both signify the growing influence of thermal fluctuations. At $k_BT/(J_\pm S^2) = 0.2$, $\arg\langle N\rangle$ is nearly stationary and very close to 0, which suggests that the thermal fluctuations dominate over the non-EQ potential from optical magnons. This is clearly seen in the histogram of $\arg O$ [Fig. 4(c)]: initially at a single ψ_2 state, the system escapes to other ψ_2 states at late time. Since the model remains XY ordered at this temperature and hence no symmetry changes occur, we infer a crossover at temperature T^*, above which the landscape essentially reverts to being thermal. Simple dimensional analysis indicates T^* scales with the energy density deposited by the pulse.

Looking ahead, our identification of a tunable effective free-energy landscape leads to a number of interesting directions for future research. First, a more detailed analysis of the finite temperature dynamics is needed for a complete picture of the aforementioned crossover. Secondly, while we have focused on classical models, it is intriguing to see to what extent the physics discussed here has a natural analogue in the quantum realm. This would be directly applicable to quantum magnets such as $Er_2Ti_2O_7$ and $NaCaCo_2F_7$ [26–28], which hold the promise of allowing a detailed and quantitative study of thermal and/or quantum OBD effects.

Research at Perimeter Institute is supported by the Government of Canada through the Department of Innovation, Science and Economic Development Canada and by the Province of Ontario through the Ministry of Research, Innovation and Science. Research at MPI-PKS is in part supported by DFG under Grant No. SFB 1143.

*Present address: Rudolf Peierls Centre for Theoretical Physics, University of Oxford, 1 Keble Road, Oxford OX1 3NP, United Kingdom.

[1] J. G. Kirkwood, J. Chem. Phys. **7**, 919 (1939).
[2] E. Guth and H. M. James, Ind. Eng. Chem. **33**, 624 (1941).
[3] L. Onsager, Ann. N.Y. Acad. Sci. **51**, 627 (1949).
[4] B. J. Alder and T. E. Wainwright, J. Chem. Phys. **27**, 1208 (1957).
[5] F. H. Stillinger Jr. and Z. W. Salsburg, J. Chem. Phys. **46**, 3962 (1967).
[6] J. Villain, R. Bidaux, J.-P. Carton, and R. Conte, J. Phys. II (France) **41**, 1263 (1980).
[7] E. Shender, Zh. Eksp. Teor. Fiz. **83**, 326 (1982) [J. Exp. Theor. Phys. **56**, 178 (1982)].
[8] H. Kawamura, J. Phys. Soc. Jpn. **53**, 2452 (1984).
[9] C. L. Henley, Phys. Rev. Lett. **62**, 2056 (1989).
[10] R. Moessner and J. T. Chalker, Phys. Rev. B **58**, 12049 (1998).
[11] R. Moessner, Can. J. Phys. **79**, 1283 (2001).

[12] B. Douçot and P. Simon, J. Phys. A **31**, 5855 (1998).
[13] J. D. M. Champion, M. J. Harris, P. C. W. Holdsworth, A. S. Wills, G. Balakrishnan, S. T. Bramwell, E. Čižmár, T. Fennell, J. S. Gardner, J. Lago, D. F. McMorrow, M. Orendáč, A. Orendáčová, D. M. Paul, R. I. Smith, M. T. F. Telling, and A. Wildes, Phys. Rev. B **68**, 020401 (2003).
[14] J. D. M. Champion and P. C. W. Holdsworth, J. Phys. Condens. Matter **16**, S665 (2004).
[15] M. E. Zhitomirsky, M. V. Gvozdikova, P. C. W. Holdsworth, and R. Moessner, Phys. Rev. Lett. **109**, 077204 (2012).
[16] L. Savary, K. A. Ross, B. D. Gaulin, J. P. C. Ruff, and L. Balents, Phys. Rev. Lett. **109**, 167201 (2012).
[17] A. W. C. Wong, Z. Hao, and M. J. P. Gingras, Phys. Rev. B **88**, 144402 (2013).
[18] J. Oitmaa, R. R. P. Singh, B. Javanparast, A. G. R. Day, B. V. Bagheri, and M. J. P. Gingras, Phys. Rev. B **88**, 220404 (2013).
[19] P. A. McClarty, P. Stasiak, and M. J. P. Gingras, Phys. Rev. B **89**, 024425 (2014).
[20] M. E. Zhitomirsky, P. C. W. Holdsworth, and R. Moessner, Phys. Rev. B **89**, 140403 (2014).
[21] See Supplemental Material http://link.aps.org/supplemental/10.1103/PhysRevLett.119.167203 for details of analytic and numerical calculations.
[22] V. I. Arnol'd, *Mathematical Methods of Classical Mechanics*, Graduate Texts in Mathematics Vol. 60, 2nd ed. (Springer-Verlag, New York, 1989).
[23] L. D. Landau and E. M. Lifshitz, *Mechanics*, Course of Theoretical Physics Vol. 1, 3rd ed. (Butterworth-Heinemann, 1976).
[24] V. S. Maryasin, M. E. Zhitomirsky, and R. Moessner, Phys. Rev. B **93**, 100406 (2016).
[25] J. G. Rau, S. Petit, and M. J. P. Gingras, Phys. Rev. B **93**, 184408 (2016).
[26] J. W. Krizan and R. J. Cava, J. Phys. Condens. Matter **27**, 296002 (2015).
[27] K. A. Ross, J. W. Krizan, J. A. Rodriguez-Rivera, R. J. Cava, and C. L. Broholm, Phys. Rev. B **93**, 014433 (2016).
[28] R. Sarkar, J. W. Krizan, F. Brückner, E. C. Andrade, S. Rachel, M. Vojta, R. J. Cava, and H.-H. Klauss, arXiv:1604.00814.